Published in final edited form as:
Cancer Res. 2020 May 15; 80(10): 2045–2055. doi:10.1158/0008-5472.CAN-19-3067.

A Protease-Activated Fluorescent Probe Allows Rapid Visualization of Keratinocyte Carcinoma During Excision

Ethan Walker[1,†], **Yiqiao Liu**[1,†], **InYoung Kim**[3,4,†], **Mark Biro**[2], **Sukanya R. Iyer**[1], **Harib Ezaldein**[3,4], **Jeffrey Scott**[3,4], **Miesha Merati**[3,4], **Rachel Mistur**[3,4], **Bo Zhou**[1], **Brian Straight**[8], **Joshua J. Yim**[7], **Matthew Bogyo**[5,6,7], **Margaret Mann**[4], **David L. Wilson**[1,9,*], **James P. Basilion**[1,9,10,*], **Daniel L. Popkin**[3,4,*]

[1]Department of Biomedical Engineering, Case Western Reserve University, Cleveland, OH, USA

[2]Case Western Reserve University School of Medicine, Cleveland, OH, USA

[3]Department of Dermatology, Louis Stokes Cleveland Veterans Affairs Medical Center, Cleveland, OH, USA

[4]Department of Dermatology, Case Western Reserve University, Cleveland, OH, USA

[5]Department of Pathology, Palo Alto, CA, USA

[6]Microbiology and Immunology, Palo Alto, CA, USA

[7]Chemical and Systems Biology Stanford University, Palo Alto, CA, USA

[8]Akrotome Imaging Inc., Cleveland, OH, USA

[9]Department of Radiology, Case Western Reserve University, Cleveland, OH, USA

[10]Fellow, National Foundation for Cancer Research, Case Western Reserve University, Cleveland, OH, USA

Abstract

Keratinocyte carcinomas (KC), including basal and squamous cell carcinomas, are the most common human cancers worldwide. While 75% of all KC (4 million annual cases in the US) are treated with conventional excision, this surgical modality has much lower cure rates than Mohs micrographic surgery, likely due to the bread-loaf histopathological assessment that visualizes <1% of the tissue margins. A quenched protease-activated fluorescent probe 6qcNIR, which produces a signal only in the protease-rich tumor microenvironment, was topically applied to ninety specimens *ex vivo* immediately following excision. “Puzzle-fit” analysis was used to correlate the fluorescent images with histology. Probe-dependent fluorescent images correlated with cancer determined by conventional histology. Point-of-care fluorescent detection of skin

Corresponding authors: James P. Basilion, Department of Radiology at Case Western Reserve University, Wearn Bldg., RB42, 11100 Euclid Ave, Cleveland, OH 44106-5056, phone: (216)-983-3264, jxb206@case.edu**&** Daniel L. Popkin, Department of Biomedical Engineering at Case Western Reserve University Wearn Building, RB49, 11100 Euclid Ave Cleveland Ohio, 44106-5056; phone: (314)-749-3041, daniel.popkin@gmail.com.

†,*These authors made equal contributions to the work.

Disclosure of Potential Conflicts of Interest: Matthew Bogyo and James Basilion are co-founders, and Brian Straight is the CEO of Akrotome Imaging, Inc. Daniel Popkin is a scientific advisory board member for Akrotome Imaging, Inc. No potential conflicts of interest are disclosed by the other authors.

cancer had a clinically relevant sensitivity of 0.73 and corresponding specificity of 0.88. Importantly, clinicians were effectively trained to read fluorescent images within 15 minutes with reliability and confidence resulting in sensitivities of 62–78% and specificities of 92–97%. Fluorescent imaging using 6qcNIR allows 100% tumor margin assessment by generating *en face* images that correlate with histology and may be used to overcome the limitations of conventional bread-loaf histology. The utility of 6qcNIR was validated in a busy real-world clinical setting, and clinicians were trained to effectively read fluorescent margins with a short guided instruction, highlighting clinical adaptability. When used in conventional excision, this approach may result in higher cure rates at a lower cost by allowing same-day re-excision when needed, reducing patient anxiety and improving compliance by expediting post-surgical specimen assessment.

Keywords

Skin carcinoma; optical imaging; tumor margins

Introduction

Keratinocyte carcinoma (KC), including basal cell carcinoma (BCC) and squamous cell carcinoma (SCC), is the most prevalent cancer in the United States, totaling over 5.4 million diagnoses and more than 3.3 million treatments per year in 2012 (1). This translates to an average annual treatment cost of $4.8 billion, which has increased 74% since 2002–2006 (2). Treatment modalities for KC include conventional excision, Mohs micrographic surgery (MMS), electrodesiccation and curettage, radiation therapy, cryotherapy, as well as topical and oral medical therapies. MMS has the highest cure rate, and studies comparing recurrence rates of the two main surgical modalities have consistently demonstrated superiority of MMS over conventional excision in KC treatment (2.9–4.4% for MMS vs. 5.5–13.5% for conventional excision over 5–10 years (3,4). These differences are likely due to the *en face* visualization technique used during MMS that allows 100% visualization of the surgical margins in real-time, in contrast to the traditional “bread-loafing” histopathologic assessment in conventional excision that examines less than 1% of the margins. Given the excellent cure rates of MMS, its use has increased over 400% between 1995 and 2009 (5). However, MMS is not considered appropriate for all tumor types and locations and is relatively resource-intensive and difficult to perform. In fact, 75–80% of all KC are treated by conventional excision annually (5). While tumor is removed along with margins of healthy tissue to achieve clearance, incomplete tumor resection recognized during standard-of-care bread-loafing histopathological examination occurs in 4 to 16.6% of all cases (6,7). Re-excisions after conventional surgery may be associated not only with increased anxiety, inconvenience, and financial burden for patients, but also with increased healthcare costs. These limitations of conventional excision pose an unmet need for an alternative time-saving approach that could achieve higher cure rates and be easily deployed with minimal training.

A number of non-invasive optical imaging technologies have been developed for detection of KC (8). As the oldest imaging modality, dermoscopy is a well-established technique for assessing pigmented skin lesions (9) but the level of expertise significantly affects diagnostic

accuracy of KCs (10). Conventional light microscopy is restricted to being performed on very thin tissue specimens because human skin is optically turbid, scattering and absorbing visible light to a high degree (11). This obstacle may be overcome by near-infra red (NIR)-based two-photon laser scanning microscopy, because of decreased scatter and absorption. However, effective matching is difficult and significant aberration remains, even when using objectives equipped with correction collars (12) resulting in overall sensitivity of 84% and overall specificity of 76% in a non-clinically optimized format (13). Pooled data from studies using optical coherence tomography (OCT) alongside visual inspection and dermoscopy for the detection of KCs estimated a sensitivity of ~95% and specificity of ~77% (14–16). However, OCT is costly, limited in imaging deeper tumors, and signals are difficult to interpret (17). Using Raman spectroscopy 100% sensitivity and 91% specificity in discriminating KCs from normal skin was reported (18). However, sensitivities between 95–99% and specificities between 15–54% were also reported (19), reflecting the suboptimal shallow signal depth and narrow field of this tedious imaging technique.

Others have used auto-fluorescence emission of BCC and SCC to differentiate cancer from surrounding normal tissue (20), however, areas defined as tumor according to auto-fluorescence images are 2 to 3-fold larger than the actual tumor size based on traditional H&E staining, thereby limiting its tumor delineation applications (20). Metabolized to fluorescent protoporphyrin-IX, 5-aminolevulinic acid (5-ALA) has been investigated to discriminate cancer using fluorescence. 5-ALA demonstrated pooled 90–95.4% sensitivity and 80–88.6% specificity in KC detection (21,22). However, subclinical extension common to high-risk cutaneous SCC often goes undetected with 5-ALA. This lack of fluorescence in larger lesions may be related to limited accumulation of 5-ALA (23). This technique is also time consuming, labor intensive, and has side effects: pain, edema, pustules, itching, epithelial exfoliation, and post-inflammatory hyperpigmentation. Some studies demonstrated reflectance confocal microscopy imaging achieved sensitivities of 92–100% and specificities of 85–97% for KC (24,25), but the approach has a high-cost and low-depth detection. Because of their limitations none of these approaches have gained general adoption for point-of-care KC removal.

Here we present a strategy to address the unmet needs and limitations of other existing non-invasive optical imaging modalities in conventional KC treatment using a protease activated “smart probe” that rapidly and reliably identifies tumor margins to guide the surgeon in real-time. In recent years, optical fluorescence-guided surgery has emerged as a promising non-invasive tumor detection modality contributing to improving oncologic care in solid organ tumors (26–28). However, its utility in skin cancer detection has yet to be demonstrated. Previously, we demonstrated that topical application of a fluorescent imaging agent detected cancer-associated cathepsin activity from the dermal side of debulked SCC and BCC samples with 99% sensitivity and 89% specificity, all within minutes (29). In that study, a quenched activity-based probe (qABP), GB119 (30), which covalently targets cysteine cathepsin proteases that are overexpressed in human skin cancers (31–33), was utilized. Covalent binding of GB119 to endogenous target proteases results in de-quenching and activation of fluorescence, which is then captured by an imaging system (34,35). The qABPs are highly selective and have been shown to be very effective for imaging tumor-expressed proteases (30,36,37). Here we report utilization of an enhanced imaging system that allows

minimal light scatter coupled with a NIR quenched protease probe 6qc-NIR that reduces auto-fluorescence, with overall higher performance in cancer visualization. The 6qcNIR probe is a hydrophobic substrate-based probe (37) that is taken up by cells and becomes activated by cathepsin cleavage inside lysosomes creating a charged molecule that cannot leave the cells.

We believe that our approach may complement current noninvasive optical imaging technology for KC detection and/or provide better value given lower setup costs, deeper signal penetration and simpler signal interpretation.

Materials and Methods

Collection of human skin specimens

Between January 31, 2017 to June 12, 2018, 90 patients referred to the Veterans Affairs (VA) Dermatology excision clinic with biopsy-proven BCC and SCC were included in the study. Participants in the study gave written informed consent; the study was conducted in accordance to international ethical guidelines (Declaration of Helsinki) and done in compliance with the VA Louis Stokes Cleveland Medical Center Institutional Review Board (protocol #16066-H46). Elliptical excision was performed on biopsy-proven SCC or BCC with 4–5-mm margins. Immediately after resection, the specimen was placed in saline to prepare for image capture, as outlined below.

Ex vivo imaging of human skin specimens

Immediately after excision, the skin specimen was brought to the laboratory which was set up in a room next to the operating room. The specimen was rinsed by sterile saline to delete debris, fresh blood, and blood clots and then blotted dry with gauze followed by bright-field photography. Then baseline NIR fluorescent images were obtained. Next, a paper applicator impregnated with 6qcNIR (10-μM) dissolved in 100% dimethyl sulfoxide was applied to the epidermal side of the specimen followed by wrapping with lab-film. After 10–15 min incubation, the applicator was taken off, excess probe was rinsed from the sample with saline followed by fluorescent imaging. All NIR-fluorescent images were taken and analyzed by a flying-inverted-spot fluorescent 800-nm Odyssey-CLx commercially available scanner and Image-Studio™ software (all Li-Cor Biosciences). Next, the specimen was placed in formalin and sent to pathology. The next day, a half of the dermal side and edge (12–6 o'clock) along with another half and edge (6–12 o'clock) of the same specimen were marked in black and blue ink, respectively, by pathology. No changes were made to standard-of-care excision.

"Puzzle"-fit" analysis to correlate fluorescence to histology

Image registration, reconstruction, and alignment of histopathological images to 6qcNIR fluorescence images was performed to overlay cancer H&E annotations on the post-probe fluorescence images. Detailed steps of this method have been described (38) and are given in the Supporting Information.

Intensity-based objective sensitivity and specificity analysis using detection of cancer based on fluorescence intensity

We used fluorescence intensity thresholds to detect KC using a receiver operating characteristic (ROC) curve analysis with each "puzzle-fit" histology line (38) as one object. The "puzzle-fit" process allowed accurate overlay of cancer H&E annotations on the post-probe fluorescence images and is detailed in Supporting Information.

The histology lines depicting location of histology sections were categorized using the following rules: true positive (TP) – dilated ROIs intersected a histology line with cancer and touched the cancer region, true negative (TN) – no dilated ROIs intersected a histology line with cancer, false positive (FP) – dilated ROIs intersected a histology line without cancer, and false negative (FN) – either no dilated ROIs intersected a histology line with cancer or the dilated ROIs intersected a histology line with cancer and included only the non-cancer region. A threshold for cancer from 50 to 1,000 with a step size of 50 was swept for ROC analysis using the 75^{th} percentile intensity value for each ROI. The number of TP, TN, FP, and FN lines was computed for each threshold along with sensitivity and specificity, which provided a point on the ROC.

The ROC curve was analyzed numerically to determine the area under the curve (AUC), our Fig. of merit for detection. Our ROC analysis should not be confused with traditional ROC analysis in medical imaging where the reader is given the whole image or a known lesion location to score, or free-response ROC (FROC) where the reader must identify correctly a lesion location in an image and then score it. In our case, cancer/no-cancer is known at only sparse locations where there is histology; hence, we chose to analyze histology lines rather than images.

Blinded physician "Reader Study"

To assess whether trained readers are able to differentiate cancer from normal tissue on 2D-fluorescent probe images, three dermatologists were recruited. ROC analysis (39) was utilized and the analysis is similar to the intensity-based objective study except that candidate ROIs were annotated by three dermatologists, detailed in Supporting Methods.

Evaluation of reader responses regarding intensity

For one reader, we analyzed intensities corresponding to TP and FP annotations over the 90 samples to determine if they were using intensity as a cue. We generated box plots with the central mark indicating the median, and the bottom and top edges of the box indicating the 25^{th} and 75^{th} percentiles, respectively.

Results

Workflow and study design

A representation of the study workflow is depicted in Fig. 1. After conventional excision of a biopsy-proven KC, bright-field and fluorescent images were captured. After incubation with the 6qcNIR probe, fluorescent images were captured again and overlaid against the bright-field photo. To help identify the pieces after sectioning, a diagonal score was applied to the

specimen via scalpel and filled with black ink to create a fiduciary to assist in lesion localization. Per standard-of-care, the excision specimen underwent formalin fixation and was sectioned transversely into bread-loaf pieces. Each transverse section was numbered from sequentially (range=6–24 sections; median=13 sections) and photographed with all pieces in sequential order. "Puzzle-fit" analysis (38) was applied to digitally bring the bread-loaf sections together into a single image that was overlaid onto the fluorescent image, and finally onto H&E sections highlighting areas of histopathological tumor positivity. To validate the clinical adaptability of this technology, fresh tissue and fluorescent images were presented to dermatologists, blinded to the clinical record who were asked to determine likelihood of tumor from fluorescence images.

Characterization of patients and specimens

A total of 90 specimens were evaluated, including 56 SCC and 34 BCC. Histopathological subtypes, time from biopsy to excision, anatomic locations of tumors, and demographics of patients are outlined in Supplementary Tables S1 and S2. The most frequent SCC subtype was well-differentiated, constituting 82.1% of SCC specimens and 51.1% of all cancer specimens. The most frequent BCC subtype was nodular, constituting 26.5% of BCC specimens and 11.1% of all cancer specimens. Mean time from biopsy was 48.46±28.35 days. All patients were voluntarily enrolled sequentially from the Louis Stokes VA Clinic and were Caucasian males. Most patients were within 66–75 years of age (n=55), followed by 76–85 years of age (n=18), <65 years of age, (n=11) and >86 years of age (n=6). Of 90 total specimens, histology revealed cancer in 29 of 90, or 32.2% of all specimens. As shown in Supplementary Table S1, 29.3% of well-differentiated and invasive SCC specimens and 33.3% of nodular BCC subtypes had residual cancer.

Gross correlation of fluorescent signals with histology

Bread-loafing histopathologic assessment demonstrated no residual tumor in 67.8% of the specimens. In these specimens, no fluorescent signal was detected (Fig. 2A). In specimens that demonstrated a strong fluorescent signal following 10-min of incubation with 6qc-NIR (n=29, 32.2% of all specimens), conventional histopathological examination revealed the presence of residual tumor that correlated with positive fluorescence for both SCC and BCC (Fig. 2B and 2C).

Co-localization of histopathologic tumor positivity and fluorescence using "puzzle-fit" analysis

Conventional histopathologic assessment allows tumor visualization from the horizontal plane, obtained by sectioning the specimen into 2–3 mm transverse "bread-loaf" slices. In contrast, fluorescence imaging with 6qc-NIR is captured *en face*, which is the plane used in MMS to visualize all tumor margins. To reconcile the disparity in the visualization axes, we developed the "puzzle-fit" analysis – a technique that allows effective and precise histopathologic and fluorescent co-localization of the tumor with 100-μm accuracy (38). Briefly, diagonal scores are applied along the specimen (Fig. 3A and B) with a scalpel then inked in black prior to fixation in formalin (Fig. 3C–F, black lines), which can be identified as a single area of concavity on each histopathologic bread-loaf section. Using the "puzzle-fit" software (38) transverse sections are digitally brought together to reconstruct the

elliptical gross bright-field image, after which distances are calculated to determine the exact location of the score on the fluorescent image. Subsequently, positive tumors margins on histology (Fig. 3G, red line) can be compared to areas of strong fluorescence (Fig. 3H, red lines). This analysis allowed high-accuracy correlation of fluorescence to histology. The "puzzle-fit" accuracy calculated using Euclidean distances between epidermal surface landmarks on registered fixed tissue and fresh tissue was 0.48±0.39 mm. Extrapolated with a linear model, the accuracy on the 100-μm margin was ~100-μm, enabling unambiguous visual interpretation of the results. Using this methodology, fluorescence cancer signals corresponded spatially with histopathological annotations.

Detection of previously overlooked tumor by 6qcNIR

Since fluorescent imaging allows contiguous visualization of the tissue without skipped areas, we hypothesized that our smart probe technology may fill the gap in the key limitation of bread-loafing histology in which less than 1% of the margins are visualized (40). As hypothesized, 6qc-NIR was able to detect tumor in specimens that were initially noted to be "clear of tumor" by histology (Fig. 4A–D). Initial histopathological assessment revealed that no residual tumor was present in the conventional excision sample (Fig. 4E). "Puzzle-fit" analysis revealed that bread-loaf sectioning did not transect but was performed right adjacent to the presumed residual tumor represented by the fluorescence (Fig. 4C). With high suspicion for tumor presence given the radially-spreading fluorescent signal in the center, deeper histopathological sections were requested. Indeed, further sectioning that transected the tumor confirmed the histopathological presence of tumor (Fig. 4F). Histopathological tumor positivity correlated to the fluorescent signal rendered by 6qc-NIR when aligned by "puzzle-fit" analysis (Fig. 4D). In our hands in this small sample set, there were 2 such cases (2.2%) where 6qc-NIR detected tumors previously overlooked by histology.

Non-tumor-related fluorescence and false negative fluorescence

Incidental benign lesions stated by clinician secondary to size and present when reviewing fresh tissue images in two cases demonstrated that inflammatory lesions could generate fluorescence (i.e., seborrheic keratosis (SK) and cyst, Supplementary Fig. S1). Three BCC lesions were un-detected (FN) (Supplementary Fig. S2) and strong fluorescence signals were seen in some non-cancerous lesions (FP), including foreign body granuloma (n=1), epidermal inclusion cyst (n=1), SK (n=4) (Supplementary Fig. S3A–C), and healing wounds associated with inflammation (n=14) (Supplementary Fig. S3D). While cathepsins are highly upregulated in a tumor microenvironment, elevations may also be seen in non-cancerous inflammation leading to activation of the qABP (29,30,34). For example, in specimens that had inflammation due to wound healing (Fig. 5), the fresh tissue images revealed a prominent overlying scab at the site of previous biopsy (Fig. 5A). Thus, we hypothesized that removal of the adherent macrophage and neutrophil-laden keratinocytes would lead to decreased fluorescence that was detected initially (Fig. 5B and C). Indeed, when the adherent scab was removed (Fig. 5D), the bright fluorescence in the center was no longer present as seen in a representative sample (Fig. 5E and F). Pathology confirmed absence of tumor (Fig. 5G).

Intensity-based objective sensitivity and specificity analysis

Of 90 total samples, there were 60 histology lines with cancer and 1,115 lines without cancer. The receiver operating characteristic (ROC) curve for intensity-based, objective cancer detection gave an area under the curve (AUC) of 0.83 (Fig. 6A). At the highest recorded sensitivity of 0.78, the corresponding specificity was 0.80. The optimal Youden Index cutoff point was identified by the blue arrow on the plot (Fig. 6A), rendering a sensitivity of 0.73 and specificity of 0.88. This point corresponded to an intensity threshold of 250 gray-scale units where the maximum intensity in a sample was ~5,000.

Clinical evaluation: “Reader Study”

Next, we sought to determine whether this technology can be easily incorporated into clinical practice by training clinicians to read fluorescent images. Representative annotations performed by three readers are shown in Fig. 6B. “TP” samples were assigned as those that have histology-confirmed tumor positivity and reader confidence of 3–5 (far left column: upper row, confidence 4 out of 5 (4/5) and lower row, confidence 5/5). “FP” samples were assigned as those having histology-confirmed tumor negativity and high reader confidence (middle column: upper row, confidence 5/5 and lower row, confidence 3/5). In the middle column, the upper row represents fluorescence from an actinic keratosis, and the lower row represents a foreign body granuloma. “TN” samples were assigned as those that are histopathologically-confirmed tumor negative and corresponding low reader confidence of 1 or 2 (far right column: upper row, confidence 2/5 and lower row, confidence 2/5).

The ROC curves and AUC for each reader are represented in Fig. 6C. In the first set of analysis, all three readers had similar AUCs (0.84, 0.86, 0.85 for readers 1, 2, and 3, respectively). In the second set, the AUCs were similar to the first set (0.83 and 0.84 for reader 1 and 2, respectively), but lower for reader 3, which was 0.79. In this analysis, reader 2 had the highest sensitivity of 0.78 with the corresponding specificity of 0.92. Compared to the intensity-based objective sensitivity and specificity analysis (Fig. 6A), the “Reader Study” had a higher specificity (0.88 for the intensity-based objective analysis vs. 0.92 for reader analysis). The mean AUCs 95%-confidence intervals were 0.85 [0.80, 0.90] and 0.82 [0.76, 0.89] in the first and second sets, respectively. The P-value for rejecting that there is no significant difference between the two sets with random reader and random cases set-up in RJAFROC was 0.15. The P-value for rejecting that there is no significant difference between intensity-based objective detection AUC and readers’ AUC results using t-test was 0.86.

For the intensity profiles characterization (Fig. 6D), annotations from reader 3 in the first set were used to represent an average reader with similar training. Confidence rating of ≥1 was used as the detection threshold to achieve the highest sensitivity. Three FP outlier cases that could be clinically excluded, which consisted of scab, foreign body granuloma, and foreign body giant cell reaction where the fluorescence intensities were much higher (in the 75^{th} percentile intensities of 1,708, 510, and 775, respectively) than other TP and FP annotations, were excluded. Plotted in Fig. 6D are the 23 true positive annotations, 23 FP annotations, and 20 of 90 tissue backgrounds. Annotated regions had higher intensity levels compared to

the background, suggesting that intensity played a major role in the readers' annotating process.

Discussion

Key findings

We demonstrate that after topical application of a fluorescent probe, the surgical specimen can be non-invasively imaged to objectively generate *en face* images, which can be captured within minutes following conventional excision of KC. Importantly, this technology demonstrated the capacity to visualize tumor that had been missed by conventional histology. This reveals the key limitation of bread-loaf histopathological assessment, which samples less than 1% of the margins of the specimen, and the ability of this technology to overcome this limitation. The intensity-based objective analysis demonstrated the highest sensitivity to be 78% with a corresponding specificity of 80%; the optimal Youden Index cutoff point demonstrated a sensitivity of 73% and specificity of 88%. Moreover, clinicians were effectively and quickly trained to read fluorescent images with reliability and confidence, with sensitivities ranging from 62 to 78% and specificities ranging from 92 to 97%, supporting the notion that this approach could be easily deployed even in rural settings to improve conventional surgery.

Comparisons of sensitivities and specificities

Ranges of highest sensitivities and the corresponding specificities in this study were 62–78% and 80–97%, respectively (including both intensity-based objective and Reader Study values), which are lower than our previously reported sensitivity and specificity of 98% and 99%, respectively (29). This is not surprising, given that the previous study was conducted using tumor debulk specimens, which are almost always positive for tumor. In this study, approximately 70% of all specimens had no residual cancer reported on conventional histology, consistent with previously reported non-residual tumor rates of 27–85% in KC excisions (41–43). The specificity from the Reader Study was higher than the intensity-based objective analysis, suggesting that human readers may be superior in excluding FP and highlighting the utility of the pre-reading training session. Notably, AUCs in this study are comparable or superior to previously reported AUC values for commonly used imaging tests, including 62% for breast tomosynthesis and 60% for full-field digital breast mammography (44), 66% for CT pulmonary nodule detection with a diameter threshold of 3-mm (45), 79% for liver metastasis using dynamic MRI and 84% using Gadoxetic acid-enhanced MRI (46), 64% for tomosynthesis and 40% for radiography in lung nodule detection (47). By applying probe to both epidermal and dermal surfaces in future studies, sensitivity may be improved.

Clinical advantages envisioned

Perioperative patient anxiety in surgical removal of KC had been linked to increased postoperative pain and decreased patient satisfaction (48). The ability to detect tumor margins in real-time during conventional excision may curb patient anxiety and increase patient satisfaction by allowing clinicians to reassure the patient that the cancer has been cleared on the day of surgery, as opposed to days to weeks later after obtaining the

pathology report and potentially second surgeries. A 15-minute tutorial was sufficient to educate the target audience which is far less time than what is necessary to educate one to read H&E frozen sections or learn other imaging modalities such as reflectance confocal microscopy (49), albeit they could be used in tandem. In addition, our approach does not require a histology technician nor a cryostat. Importantly, eliminating these barriers supports dissemination of this technology into communities that traditionally do not benefit from sub-specialists such as Mohs micrographic surgeons.

The adoption of this fluorescent technology may be particularly useful in geographic locations with low Mohs surgeon availability. The density of Mohs surgeons varies markedly based on geography, with 82.4% of all U.S. counties, 93.5% of non-metropolitan counties, and 98.6% rural counties lacking Mohs surgeons (50). Given the striking urban-rural disparity of Mohs surgeon availability, patients in areas of low Mohs surgeon density may be more likely to be treated with standard excision for treatment of KC that are Mohs-appropriate given high-risk features and/or anatomic location. Similarly, this technology can be particularly useful in improving the care of veterans within the VA healthcare system where the clinical volunteers for this study were enrolled. The incidence of KC is higher among VA patients who often have the greatest risk factors, including sun exposure and age (51). This translates to a high cost burden, totaling over $356 million in treatment costs alone (including both KC and its precursor actinic keratosis) for fiscal year 2012 which represented approximately 2% of all VA outpatient care costs (51). The availability of MMS also varies significantly among various VA medical centers, representing a gap in skin cancer treatment, which could be reduced by the adoption of this imaging technology.

Potentially, the use of this fluorescence technology may enhance cosmesis of post-surgical scars by reducing the required margins and thus resection of healthy tissue. Current recommended surgical margins, largely established many decades ago, are 4-to-6-mm for BCC and SCC for standard excision, depending on the histopathological subtypes (52,53). The findings that the majority of specimens reveal no residual cancer on histopathological assessment (70% in this study and 27–85% in literature) (41–43,54) suggest the possibility that current recommendations for surgical margins may be greater than clinically necessary. Reducing margin sizes may be feasible with the ability to ascertain the tumor margins during surgery. With our imaging technology, the surgeon may excise around the clinically visible tumor site with initially smaller margins. Improvement of cosmetic outcomes may further contribute to reduction of patients' perioperative anxiety (55). Furthermore, same-day re-excisions may help reduce healthcare spending on skin cancer treatment. There is an immense need to decrease the burden and cost of skin cancer treatment in the US, which has escalated at staggering rates. In fact, BCC and SCC are collectively the fifth most costly dermatologic condition in the US (51). Recent estimates from the Medicare Fee-for-Service population suggest that over 3.3 million patients were treated for over 5.4 million skin cancers in 2012, costing approximately $8.1 billion a year.

Reader Study

To substantiate the clinical utility of this technology, three clinicians trained in dermatology were instructed to read 90 fluorescent images, along with corresponding clinical color

images of the excision specimens. With a short training session, each reader was able to detect cancerous fluorescence in two separate data sets, demonstrating that this technology can be effectively adopted in clinical practice. Using the cut-off optimized for highest sensitivity, Reader 3 detected 23 TP, 4 FN, 37 TN, and 26 FP samples.

We can extrapolate these results for 1,000 conventionally (non-MMS) treated patients in a clinical practice where our task would be to determine cancer at the margins. Assuming that 30% of patients had cancer at the margin (the prevalence), there would be 256 TP, 44 FN, 411 TN, and 289 FP. Presumable positives would undergo additional resection at the initial surgery. Hence, for the 523 additional resections, 256 (~50%) actually would need the additional resection. Of the 300 patients actually needing an additional resection, we would predict that 256 (85%) would be detected and would undergo re-excision at the time of initial surgery. If the paradigm was to also include histopathological evaluation, then presumably more of these cases would be detected in the second detection step. We can also compute the number of times that a patient would be called back for a second surgery in this thought experiment. With our method, there would be 44 patients called back for a second surgery as compared to 300 patients without our method, resulting in important benefits as discussed above – decreased patient anxiety, decreased cost, and increased patient compliance.

Limitations

Key limitations of this study involve non-tumor related FP fluorescence. 6qcNIR was designed to target active cathepsin proteases (56,57) expressed by certain tumor cells themselves as well as inflammatory macrophages and tumor-associated macrophages (26,35,58,59). Although the physiological function of cysteine cathepsins in macrophages had mainly been described as being confined to the endosomal pathway (60), evidence is accumulating that once they are released from activated macrophages, they may be major regulators of matrix degradation, suggesting that proteases also function in an extracellular context during the disease process (61). Increased cathepsin activity is well-documented in association with macrophage-driven tissue inflammation (62–65), and is an inherent and expected caveat with the use of a cysteine cathepsin targeted imaging probes. Therefore, clinicians can adopt practices that minimize the impact of this limitation. For example, with inspection of the skin prior to excision, granulation tissue or scab that harbors neutrophils and macrophages which can lead to non-tumor related fluorescence can be removed. An incidental lesion in the field of excision (i.e., incidental seborrheic keratosis) can also be removed prior to application of probe to prevent fluorescence from non-cancerous tissue. Another limitation is represented by 3 BCC FN samples. This may be due to the small size of the residual tumor or depth of the tumor and the inability of the probe to reach deep tumor from the epidermal side. This may be improved by applying the probe from the dermal side for conventional excisions or using a microneedle applicator to allow improved penetration of the probe from the epidermal side. Compared to the reported incomplete resection rates of 4–16%, none of our samples had residual tumor at the margins of resected tissue. This could be due to an insufficient sample size to reach the statistically reported incomplete resection rates. Also, larger biopsies may be taken in the VA population at the patients' request and clinicians' discretion to remove as much tumor as possible during biopsy, as anecdotally at

our VA a number of patients refuse further surgery or are lost to follow-up. Finally, deeper margins bearing tumor were not visualized in our study.

Here, we demonstrate the clinical utility of a cathepsin substrate-based fluorescent probe 6qc-NIR in cutaneous SCC and BCC excision for the first time. This probe reliably generates *en face* contiguous fluorescent images *ex vivo*, allowing rapid and easily interpretable intraoperative surgical margin examination. This technology demonstrated the capacity to visualize tumors that had been missed by conventional histology, exposing the key underlying sampling limitation of the current gold-standard histopathological assessment. Clinicians can be trained to effectively read fluorescent tumor margins with short guided instruction, highlighting the clinical adaptability of this probe technology. Clinical adoption of the 6qcNIR technology may add significant advantages to conventional excision by allowing enhanced sparing of normal surrounding tissue via expedited, simple tumor margin assessment, and same-day re-excisions potentially at a lower cost to the patients and the healthcare system – improving the current standard of care. This technology can lead to improvements in conventional skin cancer excision which is of value in many settings, e.g. where MMS is not readily available.

Supplementary Material

Refer to Web version on PubMed Central for supplementary material.

Acknowledgments

This research was supported by the Skin Diseases Research Center P30AR039750 (DLP, JPB), VA Merit Award IBX002719A (DLP), and NIH SBIR R44 CA180296 (BS, JPB, DLP, DLW). These contents are solely the responsibility of the authors and do not necessarily represent the official views of the NIH or other funding sources.

References

1. Rogers HW, Weinstock MA, Feldman SR, Coldiron BM. Incidence Estimate of Nonmelanoma Skin Cancer (Keratinocyte Carcinomas) in the U.S. Population, 2012. JAMA Dermatol 2015;151:1081–6. [PubMed: 25928283]
2. Guy GP Jr, Machlin SR, Ekwueme DU, Yabroff KR. Prevalence and costs of skin cancer treatment in the U.S., 2002–2006 and 2007–2011. Am J Prev Med 2015;48:183–7. [PubMed: 25442229]
3. Mosterd K, Krekels GA, Nieman FH, Ostertag JU, Essers BA, Dirksen CD, et al. Surgical excision versus Mohs' micrographic surgery for primary and recurrent basal-cell carcinoma of the face: a prospective randomised controlled trial with 5-years' follow-up. Lancet Oncol 2008;9:1149–56. [PubMed: 19010733]
4. van Lee CB, Roorda BM, Wakkee M, Voorham Q, Mooyaart AL, de Vijlder HC, et al. Recurrence rates of cutaneous squamous cell carcinoma of the head and neck after Mohs micrographic surgery vs. standard excision: a retrospective cohort study. Br J Dermatol 2019;181:338–43. [PubMed: 30199574]
5. Connolly SM, Baker DR, Coldiron BM, Fazio MJ, Storrs PA, Vidimos AT, et al. AAD/ACMS/ASDSA/ASMS 2012 appropriate use criteria for Mohs micrographic surgery: a report of the American Academy of Dermatology, American College of Mohs Surgery, American Society for Dermatologic Surgery Association, and the American Society for Mohs Surgery. J Am Acad Dermatol 2012;67:531–50. [PubMed: 22959232]
6. Rowe DE, Carroll RJ, Day CL Jr. Prognostic factors for local recurrence, metastasis, and survival rates in squamous cell carcinoma of the skin, ear, and lip. Implications for treatment modality selection. J Am Acad Dermatol 1992;26:976–90. [PubMed: 1607418]

7. Hansen C, Wilkinson D, Hansen M, Soyer HP. Factors contributing to incomplete excision of nonmelanoma skin cancer by Australian general practitioners. Arch Dermatol 2009;145:1253–60. [PubMed: 19917954]
8. Rajadhyaksha M, Marghoob A, Rossi A, Halpern AC, Nehal KS. Reflectance confocal microscopy of skin in vivo: From bench to bedside. Lasers Surg Med 2017;49:7–19. [PubMed: 27785781]
9. Campos-do-Carmo G1, Ramos-e-Silva M. Dermoscopy: basic concepts. Int J Dermatol 2008;47:712–9. [PubMed: 18613881]
10. Reiter O, Mimouni I, Gdalevich M, Marghoob AA, Levi A, Hodak E, et al. The diagnostic accuracy of dermoscopy for basal cell carcinoma: A systematic review and meta-analysis. J Am Acad Dermatol 2019;80:1380–8. [PubMed: 30582991]
11. Richards-Kortum R, Sevick-Muraca E. Quantitative optical spectroscopy for tissue diagnosis. Annu Rev Phys Chem 1996;47:555–606. [PubMed: 8930102]
12. Lo W, Sun Y, Lin SJ, Jee SH, Dong CY. Spherical aberration correction in multiphoton fluorescence imaging using objective correction collar. J Biomed Opt 2005;10:034006. [PubMed: 16229650]
13. Dimitrow E, Ziemer M, Koehler MJ, Norgauer J, König K, Elsner P, et al. Sensitivity and specificity of multiphoton laser tomography for in vivo and ex vivo diagnosis of malignant melanoma. J Invest Dermatol 2009;129:1752–8. [PubMed: 19177136]
14. Markowitz O, Schwartz M, Feldman E, Bienenfeld A, Bieber AK, Ellis J, et al. Evaluation of Optical Coherence Tomography as a Means of Identifying Earlier Stage Basal Cell Carcinomas while Reducing the Use of Diagnostic Biopsy. J Clin Aesthet Dermatol 2015;8:14–20.
15. Ulrich M, von Braunmuehl T, Kurzen H, Dirschka T, Kellner C, Sattler E, et al. The sensitivity and specificity of optical coherence tomography for the assisted diagnosis of nonpigmented basal cell carcinoma: an observational study. Br J Dermatol 2015;173:428–35. [PubMed: 25904111]
16. Mogensen M, Joergensen TM, Nurnberg BM, Morsy HA, Thomsen JB, Thrane L, et al. Assessment of optical coherence tomography imaging in the diagnosis of non-melanoma skin cancer and benign lesions versus normal skin: observer-blinded evaluation by dermatologists and pathologists. Dermatol Surg 2009;35:965–72. [PubMed: 19397661]
17. Schwartz M, Levine A, Markowitz O. Optical coherence tomography in dermatology. Cutis 2017;100:163–166. [PubMed: 29121130]
18. Lieber CA, Majumder SK, Ellis DL, Billheimer DD, Mahadevan–Jansen A. In vivo nonmelanoma skin cancer diagnosis using Raman microspec- troscopy. Lasers Surg Med 2008;40:461–7. [PubMed: 18727020]
19. Lui H, Zhao J, McLean D, Zeng H. Real-time Raman spectroscopy for in vivo skin cancer diagnosis. Cancer Res 2012;72:2491–2500. [PubMed: 22434431]
20. Brancaleon L, Durkin AJ, Tu JH, Menaker G, Fallon JD, Kollias N. In vivo fluorescence spectroscopy of nonmelanoma skin cancer. Photochem Photobiol 2001;73:178–83. [PubMed: 11272732]
21. Kamrava SK, Behtaj M, Ghavami Y, et al. Evaluation of diagnostic values of photodynamic diagnosis in identifying the dermal and mucosal squamous cell carcinoma. Photodiagnosis Photodyn Ther 2012;9:293–8. [PubMed: 23200008]
22. Liutkevici€ute–Navickiene J, Mordas A, Simkute S, Bloznelyte–Plesniene L Fluorescence diagnostics of skin tumors using 5-aminolevulinic acid and its methyl ester [in Lithuanian]. Medicina (Kaunas) 2009;45:937–42. [PubMed: 20173396]
23. Sandberg C, Halldin CB, Ericson MB, Lark€o O, Krogstad AL, Wennberg AM. Bioavailability of aminolaevulinic acid and methylaminolaevulinate in basal cell carcinomas: a perfusion study using microdialysis in vivo. Br J Dermatol 2008;159:1170–6. [PubMed: 18717673]
24. Nori S, Rius-Dιaz F, Cuevas J, Goldgeier M, Jaen P, Torres A, Gonzalez S. Sensitivity and specificity of reflectance-mode confocal microscopy for in vivo diagnosis of basal cell carcinoma: A multicenter study. J Am Acad Dermatol 2004;51:923–30. [PubMed: 15583584]
25. Horn M, Gerger A, Koller S, Weger W, Langsenlehner U, Krippl P, et al. The use of confocal laser-scanning microscopy in microsurgery for invasive squamous cell carcinoma. Br J Dermatol 2007;156:81–4. [PubMed: 17199571]

26. Luo S, Zhang E, Su Y, Cheng T, Shi C. A review of NIR dyes in cancer targeting and imaging. Biomaterials 2011;32:7127–38. [PubMed: 21724249]
27. Haque A, Faizi MSH, Rather JA, Khan MS. Next generation NIR fluorophores for tumor imaging and fluorescence-guided surgery: A review. Bioorg Med Chem 2017;25:2017–34. [PubMed: 28284863]
28. Tipirneni KE, Warram JM, Moore LS, Prince AC, de Boer E, Jani AH, et al. Oncologic Procedures Amenable to Fluorescence-guided Surgery. Ann Surg 2017;266:36–47. [PubMed: 28045715]
29. Walker E, Mann M, Honda K, Vidimos A, Schluchter MD, Straight B, et al. Rapid visualization of nonmelanoma skin cancer. J Am Acad Dermatol 2017;76:209–16. [PubMed: 27876303]
30. Blum G, von Degenfeld G, Merchant MJ, Blau HM, Bogyo M. Noninvasive optical imaging of cysteine protease activity using fluorescently quenched activity-based probes. Nat Chem Biol 2007;3:668–77. [PubMed: 17828252]
31. Jedeszko C, Sloane BF. Cysteine cathepsins in human cancer. Biol Chem 2004;385:1017–27. [PubMed: 15576321]
32. Kawada A, Hara K, Kominami E, Kobayashi T, Hiruma M, Ishibashi A. Cathepsin B and D expression in squamous cell carcinoma. Br J Dermatol 1996;135:905–10. [PubMed: 8977710]
33. Yan X, Takahara M, Xie L, Oda Y, Nakahara T, Uchi H, et al. Stromal expression of cathepsin K in squamous cell carcinoma. J Eur Acad Dermatol Venereol 2011;25:362–5. [PubMed: 20524946]
34. Cutter JL, Cohen NT, Wang J, Sloan AE, Cohen AR, Panneerselvam A, et al. Topical application of activity-based probes for visualization of brain tumor tissue. PLoS One 2012;7:e33060. [PubMed: 22427947]
35. Walker E, Gopalakrishnan R, Bogyo M, Basilion JP. Microscopic detection of quenched activity-based optical imaging probes using an antibody detection system: localizing protease activity. Mol Imaging Biol 2014;16:608–18. [PubMed: 24705781]
36. Blum G, Mullins SR, Keren K, Fonovic M, Jedeszko C, Rice MJ, et al. Dynamic imaging of protease activity with fluorescently quenched activity-based probes. Nat Chem Biol 2005;1:203–9. [PubMed: 16408036]
37. Ofori LO, Withana NP, Prestwood TR, Verdoes M, Brady JJ, Winslow MM, et al. Design of Protease Activated Optical Contrast Agents That Exploit a Latent Lysosomotropic Effect for Use in Fluorescence-Guided Surgery. ACS Chem Biol 2015;10:1977–88. [PubMed: 26039341]
38. Liu Y, Walker E, Iyer SR, Biro M, Kim I, Zhou B, et al. Molecular imaging and validation of margins in surgically excised nonmelanoma skin cancer specimens. J Med Imaging (Bellingham) 2019;6:016001. [PubMed: 30915384]
39. Chakraborty D P Recent advances in observer performance methodology: jackknife free-response ROC (JAFROC). Radiation protection dosimetry 2005;114:26–31. [PubMed: 15933077]
40. Telfer NR, Colver GB, Bowers PW. Guidelines for the management of basal cell carcinoma. British Association of Dermatologists. Br J Dermatol 1999;141:415–23. [PubMed: 10583044]
41. Yuan Y, Duff ML, Sammons DL, Wu S. Retrospective chart review of skin cancer presence in the wide excisions. World J Clin Cases 2014;2:52–6. [PubMed: 24653985]
42. Grelck K, Sukal S, Rosen L, Suciu GP. Incidence of residual nonmelanoma skin cancer in excisions after shave biopsy. Dermatol Surg 2013;39(3 Pt 1):374–80. [PubMed: 23279620]
43. Jackson JE, Kelly B, Petitt M, Uchida T, Wagner RF Jr. Predictive value of margins in diagnostic biopsies of nonmelanoma skin cancers. J Am Acad Dermatol 2012;67:122–7. [PubMed: 22088427]
44. Good WF, Abrams GS, Catullo VJ, Chough DM, Ganott MA, Hakim CM, et al. Digital breast tomosynthesis: a pilot observer study. AJR Am J Roentgenol 2008;190:865–9. [PubMed: 18356430]
45. Sahiner B, Chan HP, Hadjiiski LM, Cascade PN, Kazerooni EA, Chughtai AR, et al. Effect of CAD on radiologists' detection of lung nodules on thoracic CT scans: analysis of an observer performance study by nodule size. Acad Radiol 2009;16:1518–30. [PubMed: 19896069]
46. Lee KH, Lee JM, Park JH, Kim JH, Park HS, Yu MH, et al. MR imaging in patients with suspected liver metastases: value of liver-specific contrast agent gadoxetic acid. Korean J Radiol 2013;14:894–904. [PubMed: 24265564]

47. Vikgren J, Zachrisson S, Svalkvist A, Johnsson AA, Boijsen M, Flinck A, et al. Comparison of chest tomosynthesis and chest radiography for detection of pulmonary nodules: human observer study of clinical cases. Radiology 2008;249:1034–41. [PubMed: 18849504]
48. Chen AF, Landy DC, Kumetz E, Smith G, Weiss E, Saleeby ER. Prediction of postoperative pain after Mohs micrographic surgery with 2 validated pain anxiety scales. Dermatol Surg 2015;41:40–7. [PubMed: 25521098]
49. Navarrete-Dechent C, Cordova M, Aleissa S, Liopyris K, Dusza SW, Phillips W, at. al. Reflectance confocal microscopy confirms residual basal cell carcinoma on clinically negative biopsy sites before Mohs micrographic surgery: A prospective study. J Am Acad Dermatol 2019;81:417–426. [PubMed: 31227277]
50. Feng H, Belkin D, Geronemus RG. Geographic Distribution of U.S. Mohs Micrographic Surgery Workforce. Dermatol Surg 2019;45:160–3. [PubMed: 29620564]
51. Yoon J, Phibbs CS, Chow A, Pomerantz H, Weinstock MA. Costs of Keratinocyte Carcinoma (Nonmelanoma Skin Cancer) and Actinic Keratosis Treatment in the Veterans Health Administration. Dermatol Surg 2016;42:1041–7. [PubMed: 27465252]
52. Wolf DJ, Zitelli JA. Surgical margins for basal cell carcinoma. Arch Dermatol 1987;123:340–4. [PubMed: 3813602]
53. Brodland DG, Zitelli JA. Surgical margins for excision of primary cutaneous squamous cell carcinoma. J Am Acad Dermatol 1992;27(2 Pt 1):241–8. [PubMed: 1430364]
54. Gurunluoglu R, Kubek E, Arton J, Olsen A, Bronsert M. Nonpersistence of basal cell carcinoma after diagnostic shave biopsy: reconstruction when specimen is negative during surgery. Ann Plast Surg 2015;74:695–8. [PubMed: 25969972]
55. Kossintseva I, Zloty D. Determinants and Timeline of Perioperative Anxiety in Mohs Surgery. Dermatol Surg 2017;43:1029–35. [PubMed: 28595243]
56. Oresic Bender K, Ofori L, van der Linden WA, Mock ED, Datta GK, Chowdhury S, Li H, et al. Design of a highly selective quenched activity-based probe and its application in dual color imaging studies of cathepsin S activity localization. J Am Chem Soc 2015;137:4771–7. [PubMed: 25785540]
57. Verdoes M, Oresic Bender K, Segal E, van der Linden WA, Syed S, Withana NP, et al. Improved quenched fluorescent probe for imaging of cysteine cathepsin activity. J Am Chem Soc 2013; 135:14726–30. [PubMed: 23971698]
58. Olson OC, Joyce JA. Cysteine cathepsin proteases: regulators of cancer progression and therapeutic response. Nat Rev Cancer. 2015;15:712–29. [PubMed: 26597527]
59. Gocheva V, Wang HW, Gadea BB, Shree T, Hunter KE, Garfall AL, et al. IL-4 induces cathepsin protease activity in tumor-associated macrophages to promote cancer growth and invasion. Genes Dev 2010;24:241–55. [PubMed: 20080943]
60. Honey K, Rudensky AY. Lysosomal cysteine proteases regulate antigen presentation. Nat Rev Immunol 2003;3:472–82. [PubMed: 12776207]
61. Bromme D; Wilson S Role of Cysteine Cathepsins in Extracellular Proteolysis In: Parks WC; Mecham RP, editors. Biology of Extracellular Matrix. Vol. 2 Berlin: Springer; 2011 p. 23–51.
62. Withana NP, Saito T, Ma X, Garland M, Liu C, Kosuge H, et al. Dual-Modality Activity-Based Probes as Molecular Imaging Agents for Vascular Inflammation. J Nucl Med 2016;57:1583–90. [PubMed: 27199363]
63. Lyo V, Cattaruzza F, Kim TN, Walker AW, Paulick M, Cox D, et al. Active cathepsins B, L, and S in murine and human pancreatitis. Am J Physiol Gastrointest Liver Physiol 2012;303:G894–903. [PubMed: 22899821]
64. Withana NP, Ma X, McGuire HM, Verdoes M, van der Linden WA, Ofori LO, et al. Non-invasive Imaging of Idiopathic Pulmonary Fibrosis Using Cathepsin Protease Probes. Sci Rep 2016;6:19755. [PubMed: 26797565]
65. Li J, Hsu HC, Yang P, Wu Q, Li H, Edgington LE, et al. Treatment of arthritis by macrophage depletion and immunomodulation: testing an apoptosis-mediated therapy in a humanized death receptor mouse model. Arthritis Rheum 2012;64:1098–109. [PubMed: 22006294]

Significance

A fluorescent-probe-tumor-visualization platform was developed and validated in human keratinocyte carcinoma excision specimens that may provide simple, rapid, and global assessment of margins during skin cancer excision allowing same-day re-excision when needed.

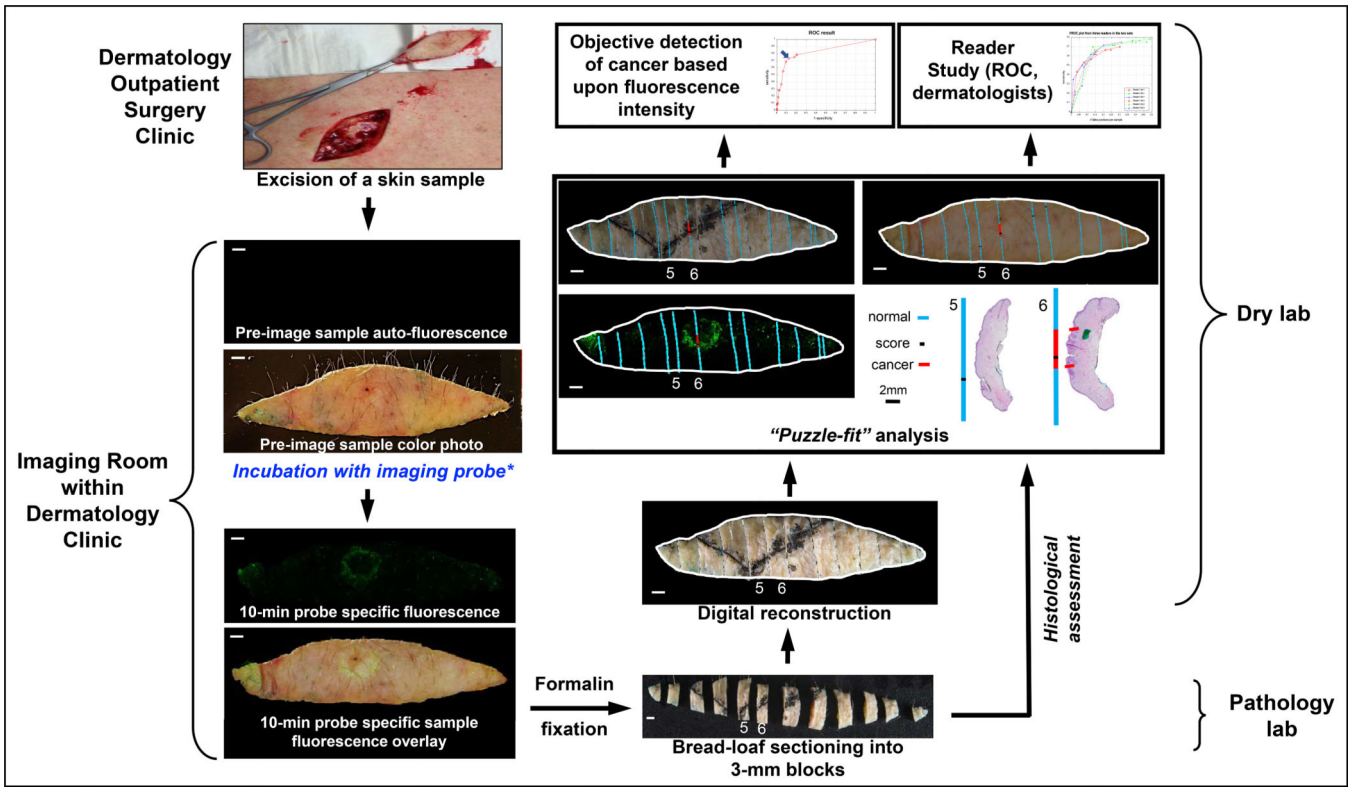

Figure 1.

Work flow and experimental design. After excision, both fresh tissue and fluorescent images were captured before and after 10-min of incubation with 6qcNIR probe. Specimen was then cut transversely into bread-loaf sections and underwent Puzzle-fit analysis to correlate the fluorescence with histology. After a 15-min training session, all fresh tissue and fluorescent images were read by blinded dermatologists in the Reader Study.

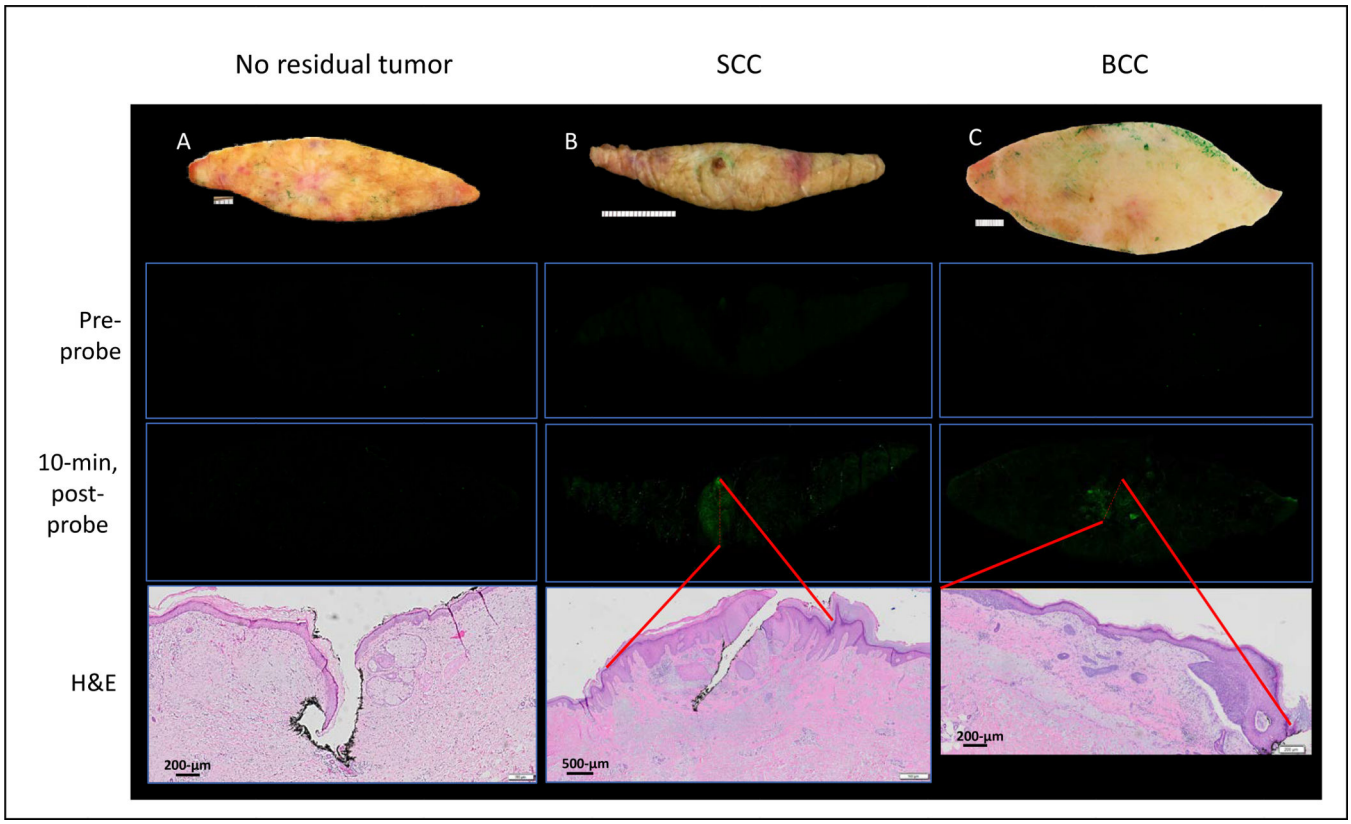

Figure 2.

Gross correlation of fluorescence with histology. Specimen noted to have no residual cancer on histology and demonstrated no detectable fluorescent signal at baseline and 10-min after probe application **(A)**. Specimens with residual SCC **(B)** and BCC **(C)** revealed areas of bright fluorescent signal that correlated with the areas of tumor present on histology (red lines mark the boundaries for SCC and BCC present on H&E and their position triangulated via fiduciaries onto the 10-min post-probe fluorescent image per Methods). H&E section represented by semi-transparent red dashed line on 10-min post-probe image.

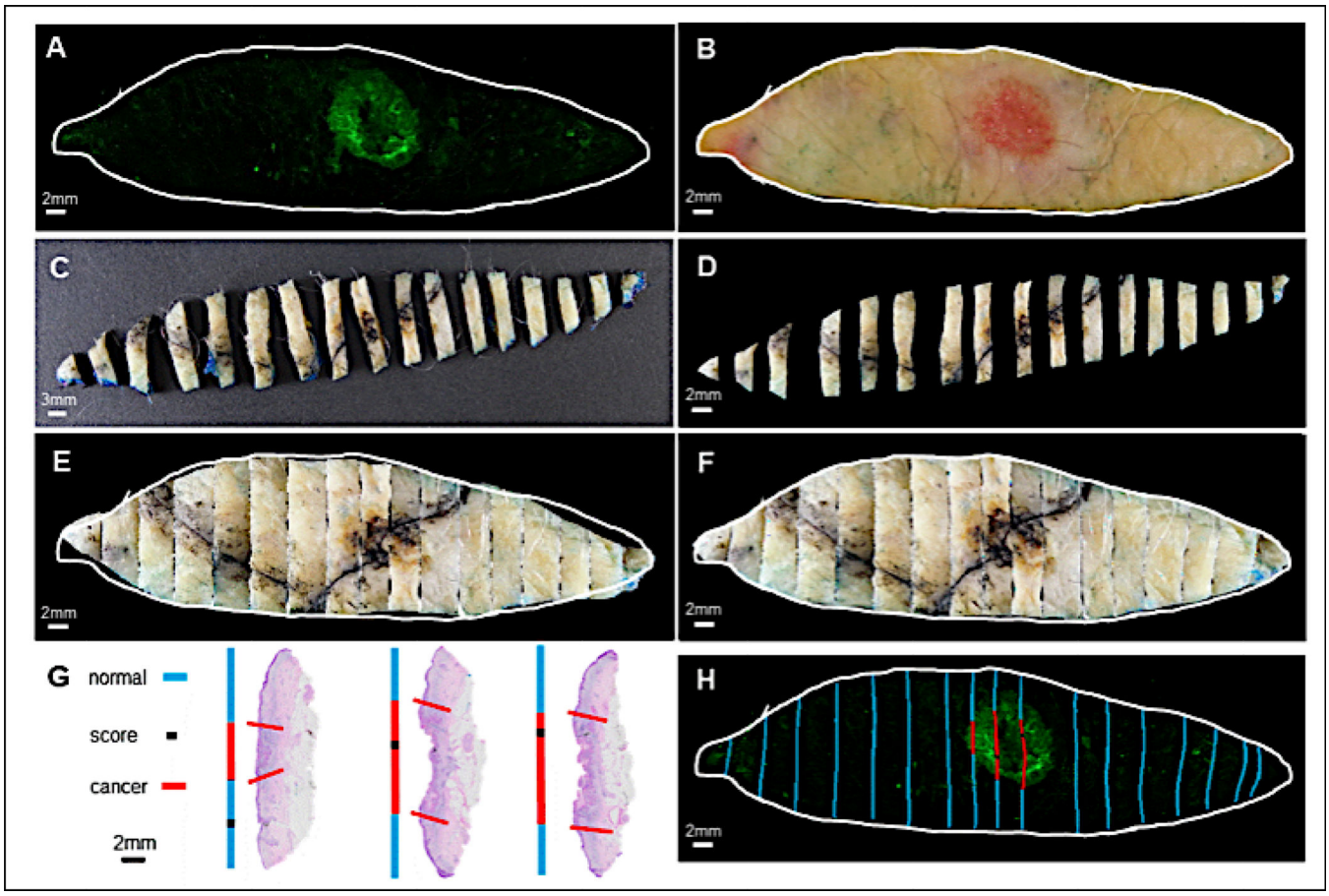

Figure 3.

Puzzle-fit analysis enables more precise co-localization of histopathological and fluorescent tumor positivity. Both post-probe fluorescent image (**A**) and fresh tissue color image (**B**) were captured immediately after incubation with 6qcNIR. After application of diagonal scores with a scalpel and black ink (black line) and formalin fixation, the specimen was sectioned into 2–3mm bread loaf slices in the pathology lab (**C**). The bread loaf slices were then segmented and adjusted to vertical alignment (**D**). After affine (**E**) and non-rigid (**F**) registration, the tissue boundary of the reconstructed bread loaf image in (**F**) aligned closely with the fresh tissue color image in (B). Each slice of the bread loaf was turned on its edge, processed, and sectioned to obtain H&E slides from the tissue blocks. Areas of cancer on each histopathological section were marked by a pathologist. Histopathological annotations were then projected onto lines in blue for non-tumor regions, red for cancer regions, and black for the scoring marks (**G**). The black scores on the reconstructed bread loaf image allowed correlation to the scores readily seen on H&E slides in (G) and further assisted in registration to the sectioned plane in the corresponding bread load slices. Finally, positive tumor regions on histology (G, red line) were compared to the post-probe fluorescent signal (**H**, red lines).

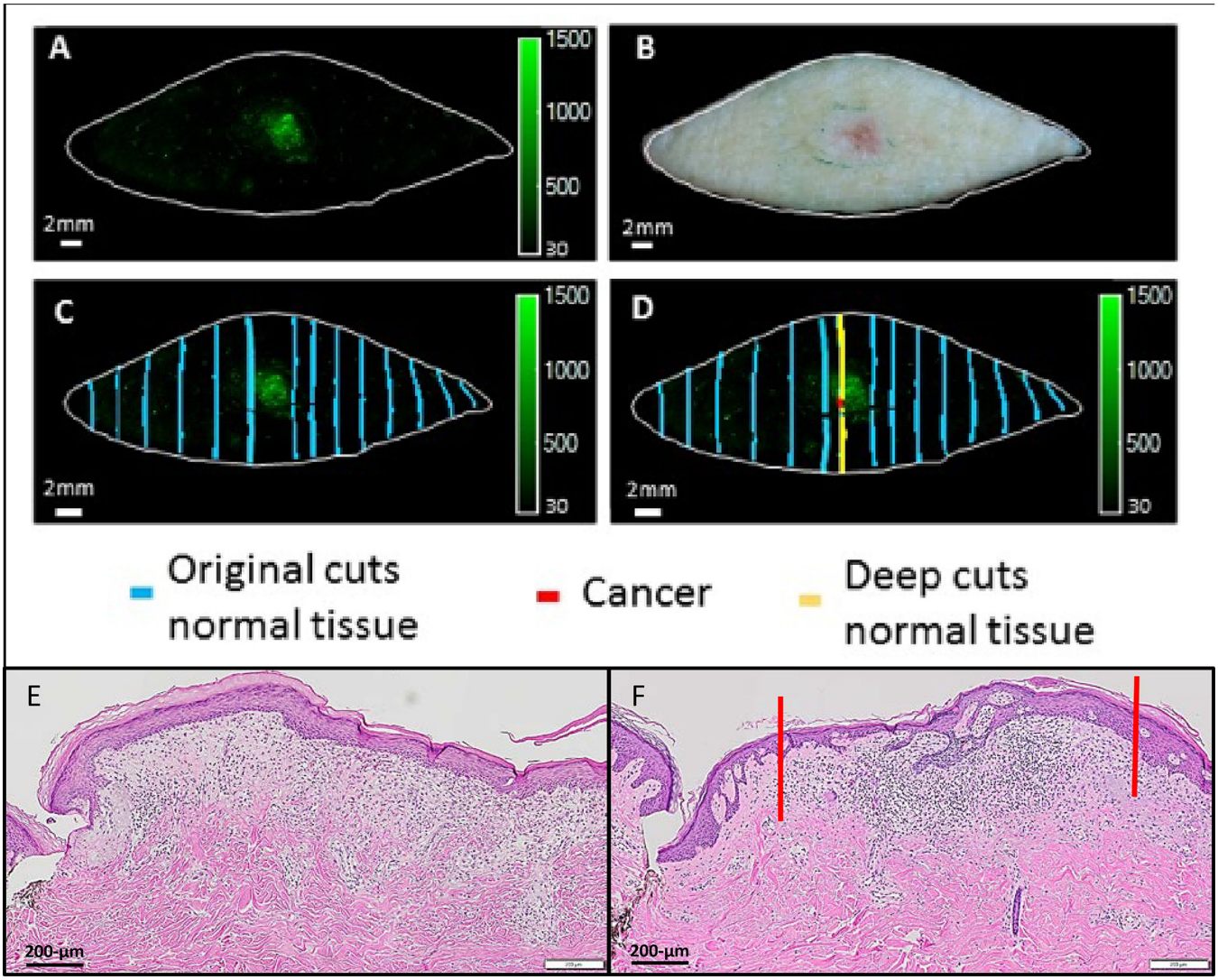

Figure 4.

Detection of previously overlooked tumor by 6qcNIR. Post-probe fluorescence image (**A**) and fresh tissue image (**B**) were captured after a basal cell carcinoma excision. Initial histopathological assessment showed no residual cancer (**E**). Puzzle-fit analysis revealed that the bread-loaf sectioning did not transect the fluorescence but was adjacent to the region (**C**). Upon further histopathologic sectioning, presence of tumor was confirmed on histology (**F**). The tumor infiltrate on histology is marked between the red lines (F), which correlates to a strong fluorescent signal rendered by 6qcNIR, marked also with a red line in **D**.

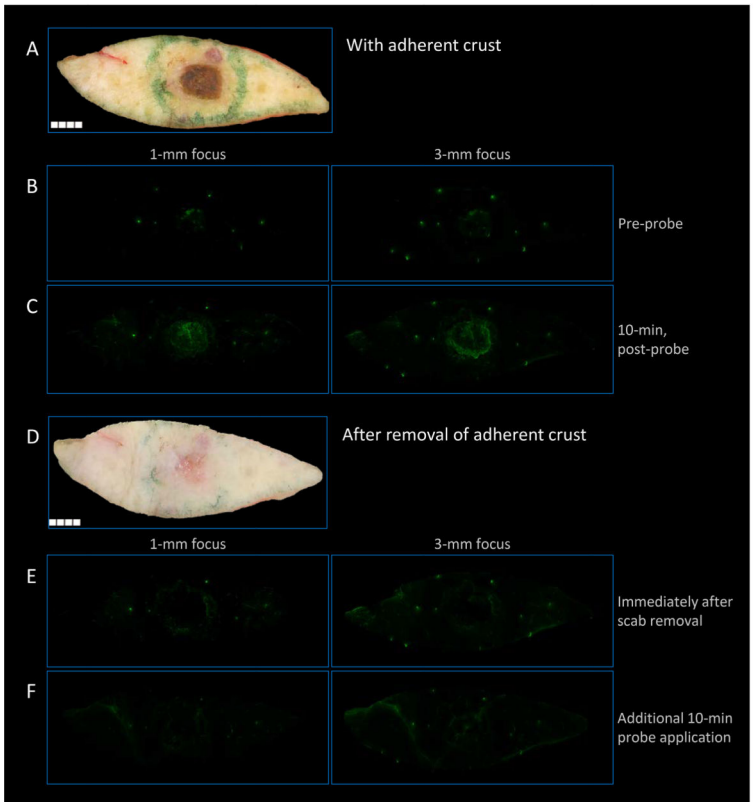

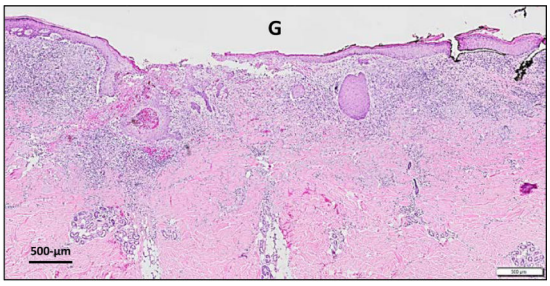

Figure 5.

False positive samples: non-tumor-related fluorescence. In specimens that had fluorescence presumably due to inflammation in a briskly healing wound, the fresh tissue images revealed a prominent overlying scab at the site of previous biopsy as in (**A**). This scab correlated spatially with fluorescence in the center, both before and after probe application (**B** and **C**). Removal of the scab (**D**) resulted in an absence of fluorescence, both before and after the application of additional probe with re-incubation (**E** and **F**, respectively). Histology demonstrating inflammatory infiltrate underlying adherent crust (**G**).

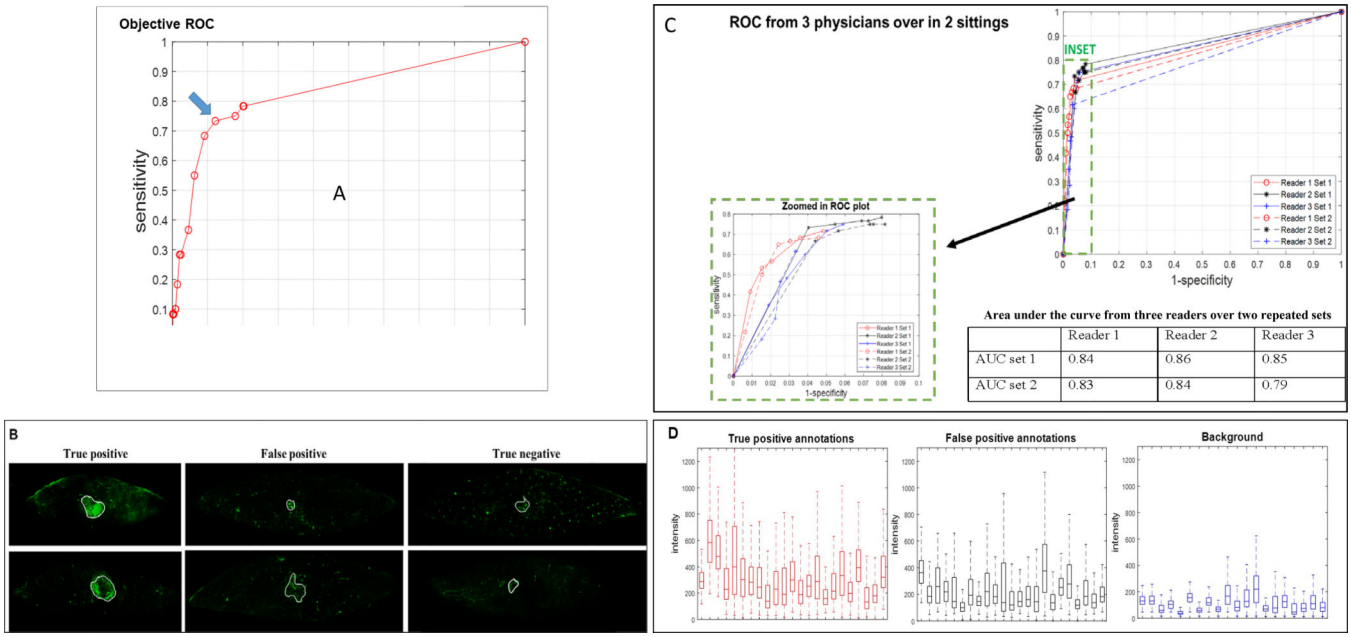

Figure 6.

Analysis of sensitivity and specificity, reader study, and fluorescence intensity. Objective ROC plot is shown plotting 1-specificity vs. sensitivity (**A**). The optimal cut point was identified by the blue arrow (A, blue arrow), corresponding to intensity threshold 250, with sensitivity of 0.73 and specificity of 0.88. Empirical area under curve was 0.83. Representative annotations performed by readers are shown in (**B**). “True positive” samples were assigned as those that have histology-confirmed tumor positivity *and* reader confidence of 3–5 (far left column: upper row, 4 out of 5 (4/5) confidence and lower row, 5/5 confidence). “False positive” samples were assigned as those with histology-confirmed tumor negativity *and* high reader confidence (middle column: upper row, 5/5 and lower row, 3/5). In the middle column, the upper row represents fluorescence from an actinic keratosis (conventionally described as a pre-cancerous lesion), and the lower row represents a foreign body granuloma. “True negative” samples were assigned as those that have histology-confirmed tumor negative and corresponding low reader confidence (far right column: upper row, 2/5 and lower row, 2/5). Reader study ROC curves from three readers over two sittings performed at least 5 days apart are shown (**C**). Due to the high specificity of the ROC results, a zoomed in ROC plot is shown as an inset for improved visualization. Empirical area under curves are 0.84, 0.86 and 0,85 for the three readers in the first set, and 0.83, 0.84, and 0.79 for three readers in the second set as shown. The highest sensitivity and corresponding specificity are 0.72/0.95, 0.78/0.92, and 0.75/0.94 for the three readers in the first set, and 0.68/0.95, 0.75/0.92, and 0.62/0.97 for the same three readers in the second set of blinded readings (C, Table). Fluorescence intensity box plots are shown for true positive and false positive annotations and tissue background (**D**).